Simulations of a scintillator compton gamma imager for safety and security

Sinclair, L.E.; Hanna, D.S.; MacLeod, A.M.L.; Saull, P.R.B.

National Research Council Canada

Conseil national de recherches Canada

Canada

Simulations of a Scintillator Compton Gamma Imager for Safety and Security

L.E.Sinclair, D.S.Hanna, A.M.L.MacLeod, and P.R.B.Saull

Abstract—We are designing an all-scintillator Compton gamma imager for use in security investigations and remediation actions involving radioactive threat material. To satisfy requirements for a rugged and portable instrument, we have chosen solid scintillator for the active volumes of both the scatter and absorber detectors. Using the BEAMnrc/EGSnrc Monte Carlo simulation package, we have constructed models using four different materials for the scatter detector: $LaBr_3$, NaI, CaF_2 and PVT. We have compared the detector performances using angular resolution, efficiency, and image resolution. We find that while PVT provides worse performance than that of the detectors based entirely on inorganic scintillators, all of the materials investigated for the scatter detector have the potential to provide performance adequate for our purposes.

I. INTRODUCTION

A requirement for innovative detection technologies to assist investigators in intelligence gathering prior to or after a radiological or nuclear incident has been identified by Canada's Chemical, Biological, Radiological-Nuclear and Explosives Research and Technology Initiative (CRTI). To address this need, we are designing a Compton gamma imager. Our design goal is a compact instrument capable of localizing a 10 mCi point source of Cs-137 40 m away to within a few degrees, in a field of view of $\pm 45^\circ$ in both directions, in under a minute.

There are other groups investigating related imager designs, employing HPGe [1], Si [2]–[4], CZT [5], or gaseous time projection chamber [6] detector technologies. These techniques generally provide superior energy- and ultimately image resolution on a per-event basis, to what can be achieved with scintillator materials. On the other hand, scintillators provide the benefit of a cost-effective way to produce a high-efficiency detector in a form which can readily be made compact and rugged, for deployment to the field. This portability constraint also introduces a need for an instrument which has low power consumption, and the cost-effectiveness of scintillator opens the possibility of deployment of more than one unit.

There is an interesting approach to hybrid Compton and coded-aperture imaging which also uses an all-scintillator design [7]. Spare parts from an all-scintillator space-borne Compton telescope have been used to demonstrate a capability

L.E.Sinclair, corresponding author, is with the Geological Survey of Canada, Natural Resources Canada, Ottawa, Ontario, Canada. Correspondence: laurel.sinclair@nrcan.gc.ca

D.S.Hanna and A.M.L.MacLeod are with the Physics Department, McGill University, Montreal, Quebec, Canada

P.R.B.Saull is with the Institute for National Measurement Standards, National Research Council, Ottawa, Ontario, Canada
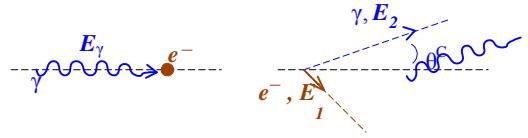
Fig. 1. Compton scatter diagram, a) initial-state and b) final-state.
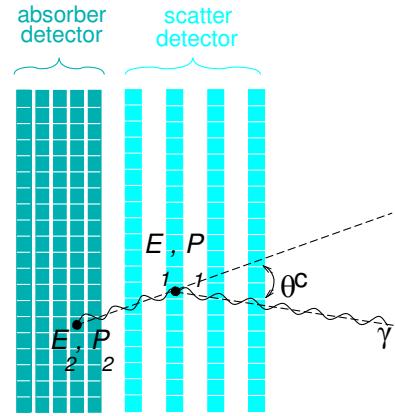
Fig. 2. Schematic diagram of a Compton gamma imager.

at ground level of identifying sources of radiation [8]. There has also been a study indicating that an all-scintillator design could be promising for the detection of highly enriched uranium [9].

Here, we present design studies conducted using the BEAMnrc/EGSnrc simulation package [10,11]. This study aims to determine whether our design goal is achievable, and whether some prospective scintillator materials can be ruled out. This work will proceed toward the development of a prototype.

II. COMPTON IMAGING

The process of Compton scattering is illustrated in Figure 1. An incoming photon of energy E_γ scatters from an atomic electron, leading to a final state in which there is an outgoing electron of energy E_1 and an outgoing photon of energy E_2.

A sketch of a Compton gamma imager is provided in Figure 2. The energy E_1 is deposited at some location in a pixellated scatter detector. The outgoing photon escapes the scatter detector to deposit its energy, E_2, at some location in a position-sensitive absorber detector. The scattering angle between the initial and final state photons, θ^C, can be determined from the two energy deposits, according to,

$$\cos\theta^C = 1 + m_0 c^2 \left(\frac{1}{E_\gamma} - \frac{1}{E_2} \right), \qquad (1)$$

where $E_\gamma = E_1 + E_2$ and $m_0 c^2$ is the electron rest energy. Thus, the position of the source may be reconstructed to lie somewhere on a cone of opening angle θ^C with its axis along the line joining the positions of the two energy deposits, and its apex at the first energy deposit. By back-projecting the cones from several events onto an image plane, an image may be reconstructed from the positions where the cones overlap.

III. DETECTOR MODELS

Using the BEAMnrc/EGSnrc Monte Carlo simulation packages we have constructed models of Compton gamma imagers. The models consist of layers of scintillator 20 cm x 20 cm in cross section, with 1 cm thickness in the scatter detector and 0.8 cm thickness in the absorber detector. Four different materials have been tested for the scatter detector, $LaBr_3$, NaI, CaF_2 and polyvinyltoluene-based plastic scintillator, hereinafter referred to as PVT[1]. In the following, the detector models will be referred to by the scatter detector material. The number of scatter detector layers is dependent upon the material.

To determine the optimal thickness of the scatter detector for each material, we looked at the probability for an incoming gamma to Compton scatter or to undergo a photo-electric process, as a function of material thickness. For this study, we have generated 10,000 events from a 662 keV 0.1 mm x 1.1 mm square parallel beam incident at the centre of the front face of a 50 cm x 50 cm x 50 cm cube of material.

The probability for an interaction to occur is presented in Figure 3 as a function of depth within the slab. For all materials, as the thickness of the material increases, the probability of at least one Compton scatter occuring, represented by the solid histogram in Figure 3, increases. However, the probability of the photon being absorbed in a photo-electric process, represented by the dotted histogram, increases with thickness as well. The probability of secondary Compton scatters also increases with material thickness (not shown). This means that there is some thickness at which the probability of exactly one Compton scatter is maximized. This probability is represented in Figure 3 by the dashed histograms.

In the models discussed here, we have chosen the material thickness of the scatter detector according to the maximum of the dashed curve in Figure 3. Thus the $LaBr_3$, NaI, CaF_2 and PVT scatter detectors feature two, three, four and eight, 1 cm-thick slabs of scintillator, respectively. There is 2 cm of spacing between the front faces of successive layers of scintillator in the scatter detector.

All of the models feature an absorber detector consisting of five 0.8 cm layers of $LaBr_3$ with 1 cm spacing between the front faces of successive layers.

The angular resolution of a Compton imager will improve, the farther apart are the energy depositions E_1 and E_2. At the same time, at least for these simple designs, the efficiency will worsen the farther apart are E_1 and E_2. In order to reduce the differences in performance which are due to these geometrical differences between the different models, we have chosen to keep the distance between the centre of the scatter detector and the front face of the absorber detector the same for all models. This distance is 9 cm, leaving air-gaps between the scatter detector and the absorber detector of various sizes for the different models, with the PVT detector having the smallest air-gap at 1 cm.

Readout devices for light collection placed between the layers will constitute dead material within the Compton imager. To account for this effect we have added a 1 mm-thick layer of SiO_2 and a 10 μm-thick layer of Au after each scintillator layer in both the scatter and absorber detectors, to represent arrays of silicon photomultipliers.

IV. EVENT SIMULATION

To compare the performance of the detectors, we simulated a mono-energetic point-source situated 40 m from the centre of the front face of the models. We investigated the energy dependence of the detector performance, choosing on-axis point sources of energy 300 keV, 500 keV, 1 MeV, 1.5 MeV and 2 MeV. We also looked at the performance for a 662 keV source located on-axis and at angles between the detector axis and the line between the centre of the front face and the source position of 10°, 20°, 30° and 40°.

We investigated three different sources of image degradation: initial-state electron physics effects, energy resolution effects, and the effect of finite detector segmentation.

- In EGSnrc, binding effects and Doppler broadening are treated according to the relativistic impulse approximation [12]. These effects are controlled by an input parameter and may easily be turned on or off.
- Smearing of the energy measurement in the scintillator and readout was applied to energy deposits in the NaI scatter detector using energy resolutions determined by experiment [13]. For all other materials, the energy deposits E_i were smeared by a Gaussian distribution about the true energy deposited, of width $C \sqrt{E_i}$, where the constant C was determined for $LaBr_3$, CaF_2 and PVT by the constraint that the FWHM resolution at 662 keV should come to 2.9%, 10% and 14% respectively[2]. To get an idea of the possible effect of underestimation of this parameter, we have simulated an additional PVT detector with a less optimistic FWHM energy resoluton of 25% at 662 keV.
- A segmentation of the detector into 1 cm^3 pixels was also simulated. When this effect is on, the energy deposit is assigned a reconstructed position at the centre of the pixel within which it took place.

[2]2.9% is a typical FWHM energy resolution at 662 keV for $LaBr_3$ quoted by suppliers. Note that suppliers do not quote typical energy resolutions at 662 keV for CaF_2 and PVT, because for these materials the high Compton to photo-electric cross section ratio means that no photopeak for Cs-137 may be observed. We chose the FWHM energy resolutions of CaF_2 and PVT based on the energy resolution of NaI, and consideration of the number of optical photons produced by these materials relative to NaI (50% and 25% for CaF_2 and PVT, respectively). Experiments with quite different geometries from ours have obtained energy resolutions in PVT ranging from 10% [14] to 25% [15]. Of course, these quantities should be determined by experiment, for the particular configuration of scintillator and light-collection device chosen, and this will be the next phase of our detector design program.

[1]Densities for these materials are taken from the technical data provided by the commercial supplier Saint Gobain. The PVT used in these simulations corresponds to Saint Gobain's general purpose scintillator BC-418.
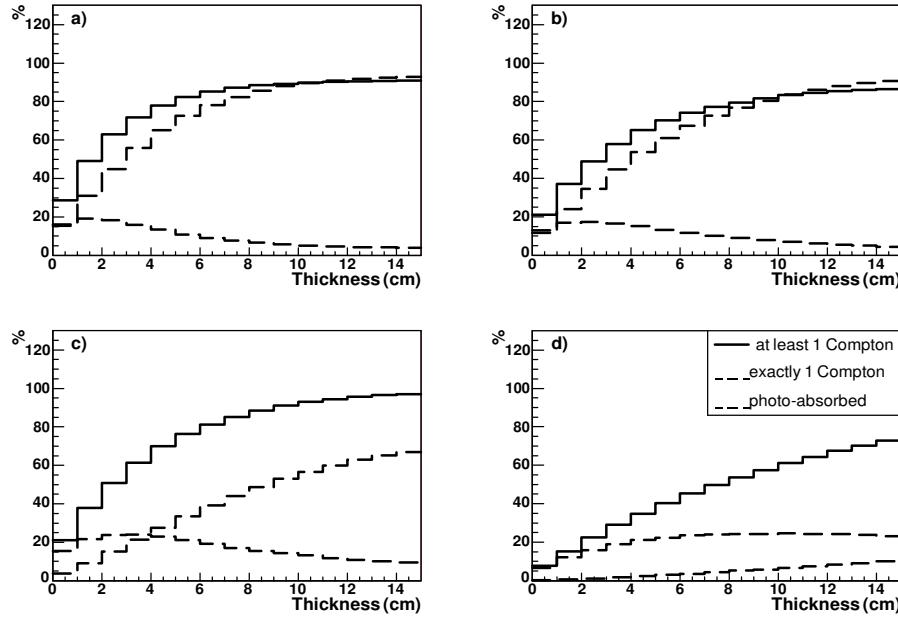
Fig. 3. Percentage of 662 keV events undergoing interaction as a function of slab thickness for a) LaBr$_3$, b) NaI, c) CaF$_2$ and d) PVT materials. The solid histogram indicates the percentage of incoming gammas for which at least one Compton scatter will occur. The dashed histogram shows the percentage which will have undergone exactly one Compton scatter. The dotted histogram shows the percentage of events undergoing a photo-electric process.

In addition, attenuation of the signal in air has been simulated by including the air between the source and the detector in the simulation.

We also included an estimate of the effect of naturally occurring radioactive material (NORM). To build up a spectrum for NORM, we followed a procedure similar to that outlined in [16]. The NORM energy spectrum had two components, a) "lines" - a set of lines representing the seven dominant energies emitted by the isotopes U-238, K-40, Th-232 and their daughters in equilibrium and b) "continuum"- a continuum distribution which is domininant at low energies and monotonically decreasing with energy. An isotropically emitting sheet of gamma rays with these raw spectra was passed through a simulation of a 4 in x 4 in x 16 in NaI "log" and then compared with data taken with that log in a laboratory. The comparison with the data was used to adjust the spectrum of the "continuum", and the ratio of "lines" to "continuum", until a reasonable representation of the low-energies and of the K-40, Bi-214 and Tl-208 peaks was obtained. An isotropically emitting sheet source with that energy spectrum was then passed through the simulations presented here.

The rate of natural background which we have observed with this log$_1$ in outdoor trials has ranged from ~ 1000 s^{-1} to ~ 1600 s^{-1}. To be conservative in our estimation of the amount of background in this study, we chose to allow that number of events to enter our model simulations which would correspond to a rate of 2000 s^{-1} in our NaI log. For 100,000 signal events, that comes to 293,460 NORM events.

For events with > 50 keV energy deposited in both the scatter and absorber detectors, and no more than one energy deposit in the scatter detector, we examined the spectra of

TABLE I
FWHM (%) OF FULL-ENERGY DEPOSITION PEAK (KEV)

Detector	Energy of source (keV)					
	300	**500**	**662**	**1000**	**1500**	**2000**
LaBr$_3$	2.9	3.7	3.2	2.4	1.9	1.7
NaI	5.1	3.3	3.4	2.9	2.6	2.4
CaF$_2$	7.7	6.2	5.1	4.3	3.6	3.3
PVT ($\sigma_E = 14\%$)	9.6	7.2	7.0	4.6	4.6	4.1
PVT ($\sigma_E = 25\%$)	12.3	12.3	10.1	7.4	7.1	6.6

the sum of the energies deposited in the scatter and absorber detectors. The spectrum obtained with the NaI model for the 662 keV source at 20° off-axis is presented in Fig. 4 a). A clear full-energy deposition peak was also observed for the other four detector types, for all energies and angles. Good fits to the peaks with the sum of a Gaussian distribution and a straight line distribution were obtained. The FWHM of the Gaussians fit to the full-energy deposition peaks for the six different source energies, for an on-axis source, are presented in Table I as a percentage. (There is little dependence of this parameter on source angle.)

Note that the FWHM energy resolutions on the total energy, as presented in Table I, are in some cases considerably better than one would expect from the smearing which has been applied to the energy deposits in the scatter detectors. This is due to the fact that most of the energy is actually deposited in the absorber detector, so the overall detector energy resolution is dominated by the energy resolution of LaBr$_3$.
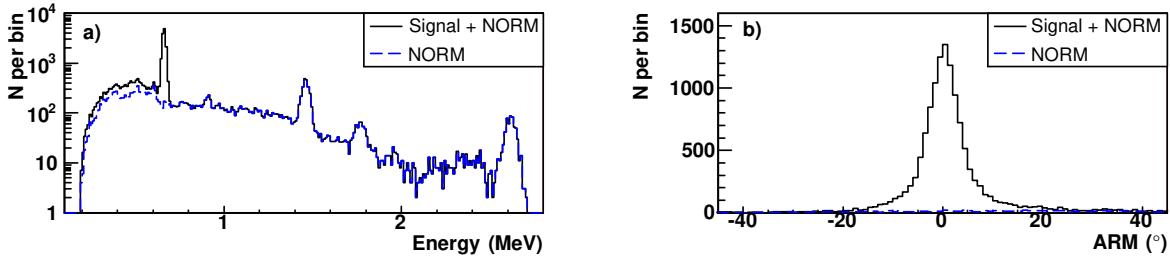
Fig. 4. For a 662 keV source at 20° off-axis and the NaI detector, for the golden event selection, a) shows the energy spectrum (leaving out the cuts on the peak energy) and b) shows the ARM distribution (including the requirement that the total energy falls within ±3σ of the peak energy). The solid histogram shows signal and NORM. The dashed histogram shows the contribution due to NORM separately.

V. RESULTS

A. Cone Reconstruction

We generated 100,000 signal events and 293,460 NORM events. "Golden" events were defined as those which satisfy:

- > 50 keV energy deposited in scatter detector,
- > 50 keV energy deposited in absorber detector,
- no more than one energy deposit in scatter detector, and
- total of energies deposited in scatter and absorber detector lying within three standard deviations of the maximum of the full-energy deposition peak.

For each golden event, we assigned the energy in the scatter detector to E_1 and the total energy in the absorber detector to E_2. The position of the energy deposit in the absorber detector was assigned to the position of the maximum energy deposit there. We then calculated the Compton cone opening angle according to Equation 1, and the angular resolution measure (ARM), the distance between the closest approach of the Compton cone back-projected onto a sphere, and the true source location.

Figure 4 b) shows an ARM distribution for a 662 keV point source 20° off-axis for the NaI model. The ARM distribution is centered on zero degrees. There is a small pedestal which is largely due to NORM. Poorly reconstructructed signal events with escaping energy or misassignment of the first and second scatters also broaden the ARM distribution and contribute to the pedestal. ARM distributions for the four other detector models look similar, with the models with poorer energy resolution exhibiting broader ARM distributions.

Figure 5 shows the FWHM of the ARM distributions for each detector model, for an on-axis point source, for four different source energies. The degradation of image resolution due to initial-state electron effects, and the effects of energy resolution and position segmentation has been added successively to the simulation. The dashed lines in Figure 5 show the result of allowing for effects such as back-scattering, which could lead to misassignment of the scatter and absorption occurrences. No additional source of image degradation is included in the dashed curves. The dotted curve shows the incremental image degradation due to including a detailed treatment of effects associated with the initial-state electron. The dash-dotted curve shows the effect of including also the smearing of energies in the scatter and absorber detectors. The solid curve is the final result for each detector. It shows the

ARM FWHM after every treated source of image degradation including segmentation of the scatter and absorber detectors into 1 cm³ pixels.

This figure illustrates several well-known effects including, a) Doppler broadening affects high-Z materials more than low-Z materials and b) both Doppler broadening and energy resolution become less of a problem as source energy increases. What is perhaps less well-known is the extent to which the smaller initial-state electron effects of the lower-Z materials can compensate for their worse energy resolution. The ARM FWHM values are comparable for all detector models at the higher energies.

Figure 5 also illustrates that the 1 cm segmentation chosen for these simulations is a reasonable value for these designs. The additional image degradation observed by setting the positions to the pixel centres is similar in magnitude to the other detrimental effects.

The FWHM of the ARM distributions are shown in Figure 6 for a 662 keV source at various angles with respect to the symmetry axis of the detector.

Our specifications call for an instrument with a wide field of view. Fig. 6 illustrates that there is very little image degradation for the models studied here, out to angles of ±40°.

Efficiency is defined as the percentage of those events which were generated in the direction of the front face of the detector, which satisfy the golden selection, and fall within three standard deviations of a Gaussian fit to the ARM distribution.

Efficiencies are shown in Figures 7 and 8, for an on-axis source of various energies and for a 662 keV source at various source angles, respectively.

In all of the studied models, the thickness of the scatter detector was chosen to optimize the acceptance of Compton events from Cs-137, which emits 662 keV gammas. It is therefore not surprising that efficiency peaks at intermediate energies for all models.

Low efficiency at 300 keV prevents our consideration of these models for Compton gamma imaging for sources of energy below 500 keV. A factor in the low efficiency is the lower energy threshold of 50 keV on the two energy deposits. This value was chosen as an estimate of a practicable lower level threshold in the final design. Variation of this threshold between 30 and 70 keV has no effect on our conclusions. With care in the eventual instrument design, it may be possible to recover some events by lowering this threshold.
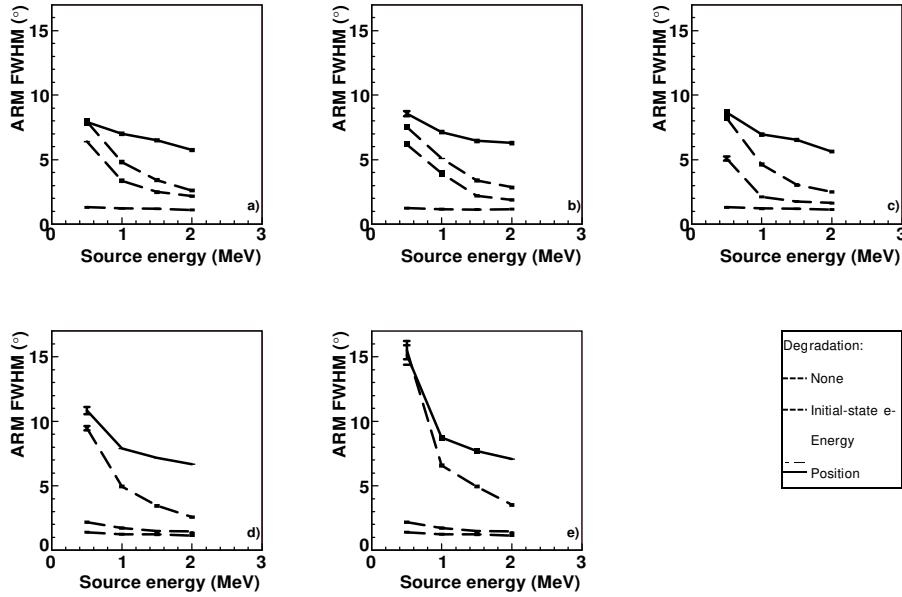
Fig. 5.   FWHM (°) of the ARM distributions for the a) $LaBr_3$, b) NaI, c) CaF_2, d) PVT ($\sigma_E = 14\%$) and e) PVT ($\sigma_E = 25\%$) detectors as a function of source energy. The dashed line shows the baseline image degradation due to event mis-reconstruction and background effects, the dotted line shows the effect of including initial state electron effects, the dash-dotted line shows the effect of including the energy resolution and finally, the solid line, shows the accumulation of all effects including the position segmentation of the detector.
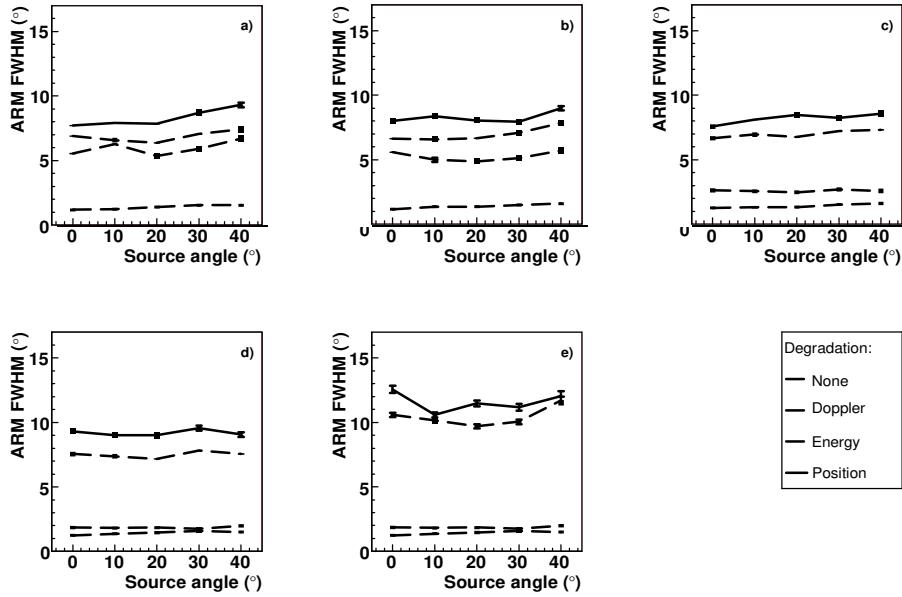
Fig. 6.   FWHM of the ARM distributions for the a) $LaBr_3$, b) NaI, c) CaF_2, d) PVT ($\sigma_E = 14\%$) and e) PVT ($\sigma_E = 25\%$) detectors as a function of source angle. The dashed line shows the baseline image degradation due to event mis-reconstruction and background effects, the dotted line shows the effect of including initial state electron effects, the dash-dotted line shows the effect of including the energy resolution and finally, the solid line, shows the accumulation of all effects including the position segmentation of the detector.

Another stringent requirement is the requirement of exactly one energy deposit in the scatter detector. It should be possible in the future to improve efficiency by reconstructing more of the events which scatter at least twice anywhere in the scatter or absorber detectors.

Efficiency is highest for the on-axis source for the low-Z detectors. The efficiency curve as a function of source angle is fairly flat for the detectors based on $LaBr_3$ and NaI, indicating that the field of view for those designs is good. The PVT detector requires a lot of material in order to initiate the first Compton scatter and this geometric effect leads to
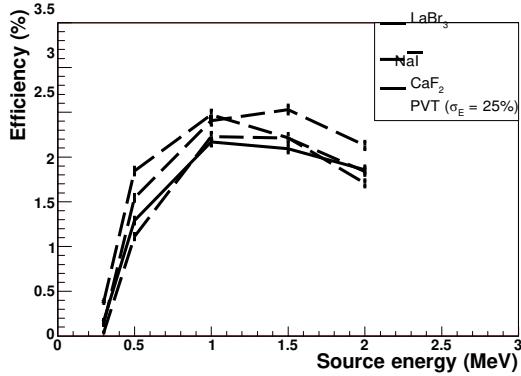
Fig. 7. Efficiency for varying source energy. The solid, dashed, dotted and dash-dotted lines show the results for the LaBr$_3$, NaI, CaF$_2$, and PVT (σ_E = 25%) detectors respectively. To reduce clutter in this plot the curve for PVT (σ_E = 14%) was left out. It falls between those of CaF$_2$ and PVT (σ_E = 25%).
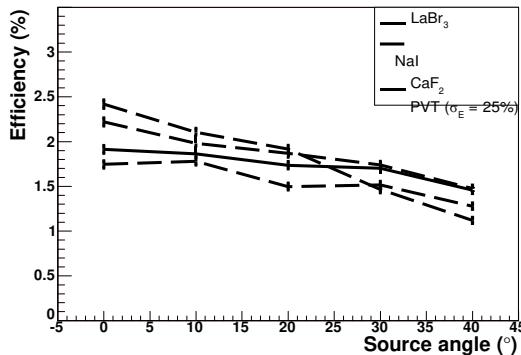

Fig. 8. Efficiency for varying angles between the line between the centre of the front face of the detector and the source, and the symmetry axis of the detector. The solid, dashed, dotted and dash-dotted lines show the results for the LaBr$_3$, NaI, CaF$_2$, and PVT (σ_E = 25%) detectors respectively. To reduce clutter in this plot the curve for PVT (σ_E = 14%) was left out. This curve parallels that of PVT (σ_E = 25%) but is 0.1 to 0.2 % lower.

the efficiency falling steeply toward the edge of the field of view. With a more clever design for a detector based on PVT, where the absorber detector surrounds the scatter detector, the efficiency could be kept high.

Note that these studies based solely on the reconstruction of the Compton scattering angles can give a lot of information about relative instrument performance and dependencies on source characteristics, but they do not directly answer the question of what image resolution can be expected in a certain period of time. That is the subject of the next section.

B. Source Position Reconstruction

As a final step in the analysis, the simulated data were passed through a position reconstruction procedure to determine the ability of each detector to locate a point source.

A standard χ^2 minimization procedure has been employed to determine the direction vector $\hat{v}(\theta, \varphi)$ which best represents the direction from the centre of the front face of the detector to the source. For N events, the following χ^2 function was constructed with two fit parameters, θ and φ, representing the

polar and azimuthal angles of the source direction vector to be determined:

$$\chi^2 = \sum_{i=1}^{N} \frac{ACA(\theta, \varphi)_i^2}{\sigma_{ACAi}} \tag{2}$$

where $ACA(\theta, \varphi)_i$ is the angle of closest approach of the direction vector $\hat{v}$ to cone i, and σ_{ACAi} is the uncertainty on this angle. To simplify the ACA expression, we have approximated the vertices of all cones as lying at the centre of the front face of the detector[3]. In this approximation, the expression for ACA becomes:

$$ACA = |\, acos\, \hat{v} \cdot \hat{r}_i - \beta^C \,| \tag{3}$$

where $\hat{r}_i$ is the unit-vector axis for cone i. Note that ACA reduces to the absolute value of the ARM for the situation where $\hat{v}$ points to the true source location.

The uncertainty on ACA, too cumbersome to reproduce here, is calculated on an event-by-event basis from the cone-axis uncertainty and the Compton opening angle uncertainty (using Equation 1), taking into account the uncertainties on the energy deposits and their positions. The effect of Doppler

tainty. The χ^2 expression was minimized using the Minuit package [17].

To extract the source direction from a given sample of events, four fit iterations are performed, with the direction determined in each iteration passed on as a starting seed direction for the subsequent iteration. For the first iteration, a preliminary estimate of the source position is deduced from the weighted mean of the cone axis directions, where for weights the squares of the opening angles are used. All events are included in the minimization procedure. In the second iteration, events having a ratio ACA/σ_{ACA} greater than five are excluded from participating in the fit. This step rejects background events and mis-identified or poorly reconstructed Compton events, but gives the fitting procedure ample freedom to find a new solution. In the third iteration, a rescan of the full set of N events is performed, but only those events with ACA/σ_{ACA} less than three are included in the fit. This provides further rejection of unwanted events, but permits events rejected from the previous iteration, where a less accurate seed direction was used, to return to good standing. The final iteration is a repeat of the third, again to take into account the more accurate starting seed vector.

This procedure was applied to three seconds of simulated data from a single 662 keV point source positioned at $\theta = 20°$ and $\varphi = -180°$ for each of the modelled detectors. The fit procedure was repeated for 100 trials. Table II shows the results. The first seven colums show average values over the 100 trials. The last two columns give the RMS spread of the fitted direction parameters. The starting number of events N for each trial is dictated by the golden-event rate for the given detector, and N_{fit} is the number entering into the final iteration of the fit. The mean χ^2/dof values are near unity

[3]This is an excellent approximation given a source at 40m from a detector of only 20 cm extent. For near sources, the adoption of a more accurate expression for ACA would permit measurement of distance.

TABLE II
AVERAGE FIT RESULTS (100 TRIALS) FOR 3 SECONDS OF ACQUISITION TIME

				Average fit results					
Det	$\overline{N}$	N_{fit}	$\overline{\chi^2/dof}$	NORM rejection	NORM impurity	$\overline{\theta}$	$\overline{\varphi}$	θ_{RMS}	φ_{RMS}
PVT25	55	50	1.08	72%	10.8%	19.8°	-179.7°	1.8°	5.7°
PVT14	51	45	1.04	56%	4.6%	20.0°	-180.0°	1.1°	4.1°
CaF2	56	46	1.23	45%	3.3%	19.9°	-180.2°	1.0°	3.1°
NaI	47	38	1.45	29%	2.0%	20.0°	-179.8°	1.0°	3.2°
LaBr3	52	40	1.55	25%	1.9%	20.1°	-179.9°	0.9°	2.8°

for both PVT detectors, for which Doppler broadening is a negligible contribution. However, the χ^2/dof values increase for the other detectors reflecting the image degradation due to Doppler broadening. The NORM rejection (impurity) column indicates the percentage of rejected (accepted) events that are background due to NORM. The mean values of θ and φ reflect an unbiased reconstruction of the source position. Their RMS values characterize how well the direction of the source can be localised. We may conclude that the fitting procedure accurately reproduces the source direction, and that there is little difference between the non-PVT detector results.

We also looked at the performance of the detector as a function of data acquisition time. For acquisition times of between two seconds and nine seconds we conducted between 500 and 100 fit trials. Figure 9 shows the percentage of fit trials for which the fitted direction was reconstructed to within 2° of the true source direction, as a function of data acquisition time. The bands show the uncertainty due to counting statistics. Except for PVT ($\sigma_E = 25\%$), all detectors are capable of correctly reconstructing the source direction most of the time even for small acquisition times. We find that LaBr3 performs the best, with only three seconds of data required to correctly reproduce the source location 90% of the time. CaF2 and NaI are about the same with four seconds required for a 90% success rate while PVT ($\sigma_E = 14\%$) and PVT ($\sigma_E = 25\%$) are at six and ten seconds, respectively. These acquisition times are well under a minute, suggesting that any of the detector options we have considered is capable of meeting the design criteria.

VI. CONCLUSION

The performance of four different all-scintillator Compton gamma imager models based on different materials for the scatter detector, has been investigated. We have obtained encouraging results from all four of the scintillators looked at, LaBr3, NaI, CaF2, and PVT. The all-LaBr3 detector is predicted to perform the best of the models studied, with NaI and CaF2 coming in a close second. Indications are that even the worst model studied, with a scatter detector composed of PVT, may be able to provide an image of a 10 mCi 662 keV source at 40 m with an RMS spread of the reconstructed source position of around two degrees, in under a minute. The next stage of this work will be to establish a test stand to validate the Monte Carlo studies experimentally.
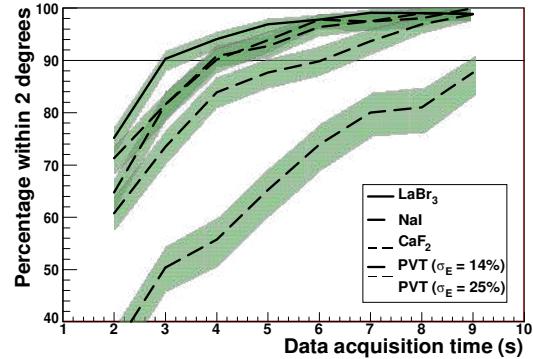

Fig. 9. Probability for correctly reconstructing the source direction to within 2°, as a function of data acquisition time. The solid, dashed, dotted, dash-dotted and long-dash dotted lines show respectively the results for the LaBr3, NaI, CaF2, PVT ($\sigma_E = 14\%$) and PVT ($\sigma_E = 25\%$) detectors. The shaded band shows the statistical uncertainty. The line at 90% is to guide the eye.

REFERENCES

[1] L. Mihailescu, K.M. Vetter, M.T. Burks, E.L. Hull and W.W. Craig, "SPEIR: A Ge Compton camera", *Nucl. Instr. Meth.*, vol. A 570, p. 89, 2007.

[2] E.A. Wulf *et al*, "Compton imager for detection of special nuclear material", *Nucl. Instr. Meth.*, vol. A 579, p. 371, 2007.

[3] K. Vetter *et al*, "High-sensitivity Compton imaging with position-sensitive Si and Ge detectors", *Nucl. Instr. Meth.*, vol. A 579, p. 363, 2007.

[4] A.S. Hoover *et al*, "Gamma-ray imaging with a Si/CsI(Tl) Compton detector", *Appl. Radiat. Isot.*, vol. 64, p. 1648, 2006.

[5] B. Smith *et al*, "An Electronically-collimated Gamma-ray Detector for Localization of Radiation Sources", *2006 IEEE Nuclear Science Symposium Conference Record*, p. 257, 2006.

[6] K. Hattori *et al*, "Gamma-ray imaging with a large micro-TPC and a scintillation camera", *Nucl. Instr. Meth.*, vo. A 581 p. 517, 2007.

[7] W. Lee, D. Wehe, "Hybrid gamma ray imaging – Model and results", *Nucl. Instr. Meth.*, vol. A 579, p. 200, 2007.

[8] J.M. Ryan, J. Baker, J.R. Macri, M.L. McConnell and R. Carande, "A Compton telescope for remote location and identification of radioactive material", *Proc. SPIE*, vol. 6943, art. 694312, 2008.

[9] B.F. Phlips, E.I. Novikova, E.A. Wulf and J.D. Kurfess, "Comparison of shielded uranium passive gamma-ray detection methods", *Proc. SPIE*, vol. 6213, art. 62130H, 2006.

[10] D.W.O. Rogers, B.A. Faddegon, G.X. Ding, C.-M. Ma and T.R. Mackie, "BEAM: A Monte Carlo code to simulate radiotherapy treatment units", *Med. Phys.*, vol. 22 (5), p. 503, 1995.

[11] I. Kawrakow and D.W.O. Rogers, "The EGSnrc Code System: Monte Carlo Simulation of Electron and Photon Transport", *PIRS-701*, National Research Council of Canada, Ottawa, Canada, 2006.

[12] R. Ribberfors, "Relationship of the relativistic Compton cross section to the momentum distribution of bound electron states", *Phys. Rev.*, vol. B 12, p. 2067, 1975.

[13] M. Moszyński *et al*, "Intrinsic energy resolution of NaI(Tl)", *Nucl. Instr. Meth.*, vol. A 484, p. 259, 2002.

[14] S.-B. Tang, Q. Ma, Z. Yin, Y. Cheng, D. Zhu, "Numerical simulation of simple position-sensitive gamma-ray detector based on plastic scintillating fiber array (OFT-06-102R1)", *Opt. Fiber Tech.*, vol. 14, p. 36, 2008.

[15] P.L. Reeder, D.V. Jordan, L.C. Todd, G.A. Warren, "Advanced Large-Area Plastic Scintillator Project (ALPS): Final Report", *PNNL-17305*, Pacific Northwest National Laboratory, Richland, Washington, USA, 2007.

[16] E.I. Novikova, B.F. Phlips, E.A. Wulf, "A γ-ray background model for Monte Carlo simulations", *Nucl. Instr. Meth.*, vol. A 579, p. 279 2007.

[17] F. James and M. Roos "Minuit - a system for function minimization and analysis of the parameter errors and correlations", *Comp. Phys. Comm.*, vol. 10, Iss. 6, p. 343 1975.